Accepted Manuscript

High temperature martensitic transformation and giant magnetocaloric effect in $Ni_{40}Co_{10}Mn_{41}Sn_9$ melt-spun ribbons

F. Chen, J.L. Sánchez Llamazares, C.F. Sánchez-Valdés, P. Müllner, Y.G. Shi, Y.X. Tong, L. Li

PII: S0925-8388(18)30532-2

DOI: 10.1016/j.jallcom.2018.02.091

Reference: JALCOM 44967

To appear in: *Journal of Alloys and Compounds*

Received Date: 10 November 2017

Revised Date: 5 February 2018

Accepted Date: 8 February 2018

Please cite this article as: F. Chen, J.L. Sánchez Llamazares, C.F. Sánchez-Valdés, P. Müllner, Y.G. Shi, Y.X. Tong, L. Li, High temperature martensitic transformation and giant magnetocaloric effect in $Ni_{40}Co_{10}Mn_{41}Sn_9$ melt-spun ribbons, *Journal of Alloys and Compounds* (2018), doi: 10.1016/j.jallcom.2018.02.091.

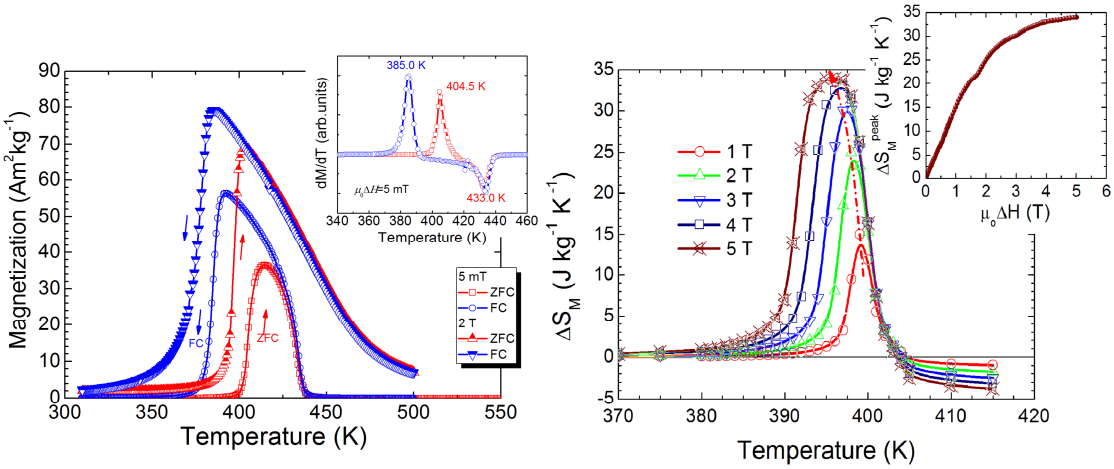

Author agreement

On behalf all authors, I will guarantee the following aspects:

(1) All authors have participated sufficiently in this work to take public responsibility for it;

(2) All authors have reviewed the final version of the manuscript and approve it for publication;

(3) Neither this manuscript nor one with substantially similar content under our authorship has been published or is being considered for publication elsewhere.

High temperature martensitic transformation and giant magnetocaloric effect in $Ni_{40}Co_{10}Mn_{41}Sn_9$ melt-spun ribbons

F. Chen[1, *], J. L. Sánchez Llamazares[2,**], C. F. Sánchez-Valdés[3], P. Müllner [4], Y. G. Shi[5], Y. X. Tong [1], L. Li[1]

[1] *Institute of Materials Processing and Intelligent Manufacturing, College of Materials Science and Chemical Engineering, Harbin Engineering University, Harbin, 150001, China.*
[2] *Instituto Potosino de Investigación Científica y Tecnológica A.C., Camino a la Presa San José 2055, Col. Lomas 4ª sección, San Luis Potosí, S.L.P. 78216, México*
[3] *División Multidisciplinaria, Ciudad Universitaria, Universidad Autónoma de Ciudad Juárez (UACJ), calle José de Jesús Macías Delgado # 18100, Ciudad Juárez, Chihuahua, México*
[4] *Micron School of Materials Science and Engineering, Boise State University, ID 83725, USA*
[5] *Department of Applied Physics, Nanjing University of Aeronautics and Astronautics, Nanjing 210016, China*

[*] Corresponding author:
Dr. Feng Chen
Institute of Materials Processing and Intelligent Manufacturing
College of Materials Science and Chemical Engineering
Harbin Engineering University
No.145 Nan Tong Street, Nan-Gang District
Harbin 150001, CHINA
Tel: +86-0451-82518173
E-mail address: chenfeng01@hrbeu.edu.cn

[**] Corresponding author:
Dr. José Luis Sánchez Llamazares
Instituto Potosino de Investigación Científica y Tecnológica A.C.,
Camino a la Presa San José 2055, Col. Lomas 4ª sección,
San Luis Potosí, S.L.P. 78216, México
Tel: +52-444-8342000
E-mail address: jose.sanchez@ipicyt.edu.mx

Abstract

We report a large magnetic entropy change associated with a high-temperature martensitic transformation in $Ni_{40}Co_{10}Mn_{41}Sn_9$ (at. %) melt-spun ribbons. The ribbons underwent a first-order forward martensitic transition and a reverse structural transition from the paramagnetic six-layered modulated martensite to a ferromagnetic austenite in the temperature range of 395-380 K. For a magnetic field change of 5 T (2 T), extremely large magnetic entropy changes of 33.9 (25) J kg^{-1} K^{-1} and 53 (22) J kg^{-1} K^{-1} upon reverse and forward martensitic transformations occurred. These values are among the largest for Ni-Mn based Heusler alloys reported so far. As compared with the large values upon heating, hysteresis losses upon cooling were negligibly low (only 0.36 J kg^{-1}). The present findings open up the possibility of elevated temperature magnetic cooling.

Keywords: Ni-Co-Mn-Sn; melt spinning; giant magnetic entropy change; high-temperature martensitic transformation; magnetic hysteresis loss.

1. INTRODUCTION

Magnetic cooling based on the magnetocaloric effect (MCE) is recognized as a new solid state refrigeration technology. It is more environmental friendly, of higher energy efficiency and of lower mechanical noise, as compared with conventional technology based on gas compression/expansion [1-3]. The discovery of giant and tunable MCE around room-temperature in $Gd_5Ge_2Si_2$ alloys et al. [4, 5], combined with the demonstration that magnetic refrigeration is a competitive room temperature cooling technology [6], boosted the search for novel materials with giant MCE and the development of magnetic cooling technology. Since then, some promising magnetic materials exhibiting giant MCE around room temperature were reported such as (Mn, Fe)$_2$P-type alloys (currently used by Haier-BASF-Astronautics in their first commercial magnetic refrigerator, a magnetocaloric wine cooler) [7, 8], La(Fe, Si)$_{13}$-based alloys (currently offered under the trademark Calorivac® by the German company Vacuumschmelze GmbH & Co, for the development of room temperature magnetic refrigerators) [7, 8], and Ni-Mn-Z (Z: group IIIA-VA elements) Heusler alloys with or without Co [9-20]. For these materials, the giant MCE is related to a coupled first-order magneto-elastic or magneto-structural transition that is accompanied by a sharp magnetization change ΔM. Up to now, most of the studies have focused on materials with a peak temperature (T_P, the temperature at which the maximum magnetic entropy change is achieved) limited below or near room temperature. Only a few reports in the literature have described the synthesis of materials with a giant maximum magnetic entropy change ΔS_M^{peak} above room temperature such as $Ni_{41}Co_9Mn_{32}Ga_{18}$ [21] (T_P = 425 K, ΔS_M^{peak} = 16.4 ± 1.8 J kg^{-1} K^{-1}) and $Ni_{37.7}Co_{12.7}Mn_{40.8}Sn_{8.8}$ [22] (T_P = 415 K, $\Delta S_M^{peak} \approx$ 15.8 J kg^{-1} K^{-1}). From the practical viewpoint, it is essential to search for new materials exhibiting a giant high-temperature MCE to extend the application range of magnetic cooling.

Among Ni-Mn-Z (Z=In, Sn, Ga and Sb) Heusler alloys, relative low cost is an important advantage for Ni-Mn-Sn alloys [23], which makes them promising candidates for commercially viable magnetic cooling. Due to the strong sensitivity of transformation temperatures to the chemical composition, their first-order structural transition may be shifted to higher temperature, such as 466 K for $Ni_{43}Co_7Mn_{41}Sn_9$ [24] and 560 K for $Ni_{43}Co_7Mn_{43}Sn_7$ [25]. Furthermore, we reported a large peak magnetic entropy change value ΔS_M^{peak} of 15.8 J kg^{-1} K^{-1} above 400 K for $Ni_{37.7}Co_{12.7}Mn_{40.8}Sn_{8.8}$ ribbons [22]. Consequently, Ni-Co-Mn-Sn alloys with an appropriate composition may exhibit a giant MCE above room temperature.

In this study, $Ni_{40}Co_{10}Mn_{41}Sn_9$ melt-spun ribbons were prepared. The bulk master alloy exhibited a magneto-structural transition at about 410 K [26]. As homogeneous element distribution obtained from rapid cooling leads to an enhanced ΔS_M (magnetic entropy change), for example in La-Fe-Si [27] and Ni-Mn-In-Co [17], a large MCE above room temperature is expected for the present ribbons. Here, we studied the microstructure, structural transition and magnetic-field-induced magnetic entropy change through both reverse and forward first-order martensitic transformation. Hereinafter, A and M are used to represent the austenite phase and the martensite phase, respectively. Therefore, the forward first-order martensitic transformation is referred to as A → M transition, and the reverse transformation as M → A transition. Above 373 K, extremely large magnetic entropy changes were achieved for both transformations upon heating and cooling.

2. EXPERIMENTAL PROCEDURE

A polycrystalline bulk alloy with a nominal composition $Ni_{40}Co_{10}Mn_{41}Sn_9$ (at. %) was arc melted using high-purity elements (> 99.9 %). The alloy was then induction melted in a quartz crucible and ejected through the circular nozzle onto the polished surface of a rotating copper wheel at a surface linear speed of 10 m/s. The average thickness of the obtained ribbons was ~40

μm and had a nearly columnar grain structure (Fig. 1). The melt-spun ribbons were sealed in vacuum quartz tubes and annealed for 1 hour at 1073 K followed by quenching into ice water. The microstructure was examined with scanning electron microscopy (SEM, Quanta 200) and transmission electron microscopy (TEM, JEOL JEM-2100 LaB_6). The TEM sample was directly subjected to twin-jet electropolishing using an electrolyte solution consisting of 10 % perchloric acid and 90 % ethanol by volume. The phase transformation was studied using a Perkin Elmer Diamond differential scanning calorimeter (DSC). Magnetization studies were carried out with vibrating sample magnetometry with an oven option of a Quantum Design PPMS® Dynacool® - 9T platform. We cut a sample with the approximate dimensions 0.7 × 3.5 mm^2 for magnetic measurements that was glued with Duco cement on the VSM oven heater stick. The major length was parallel to the length direction of the ribbon. The magnetic field $\mu_o H$ was applied along the major length of this parallelepiped sample to minimize the demagnetizing field. Owing to the strong effect of the magnetic field on the M → A phase transition, a fixed thermal protocol was followed prior to measure each isothermal magnetization $M(\mu_o H)$ curve [28]. (1) Through the M → A transition: At zero magnetic field the sample was heated to 500 K to stabilize austenite, cooled to 310 K to completely form martensite, and then heated again in no-overshoot mode to the selected measuring temperature T_{meas}. (2) Through the A → M transition: At zero magnetic field the sample was cooled down to room temperature (300 K) to stabilize martensite, heated to 475 K to completely form austenite, and then cooled again in no-overshot mode to the selected measuring temperature T_{meas}. These procedures ensure that prior to applying the magnetic field at each measuring temperature the sample exhibits the phase constitution that corresponds to the thermally induced structural transition.

3. EXPERIMENTAL RESULTS AND DISCUSSION

3.1 Microstructure and phase transformation.

Fig. 2(a) shows a SEM image of the ribbon surface. The typical lath-liked martensite indicates that the A → M transition was complete above room temperature. No traces of second phases were found, which often occur in Co-rich Ni-Co-Mn-Sn bulk samples [29]. Some martensite variants crossed a grain boundary, as marked by a dashed ellipse in Fig. 2(a), which was also observed in $Ni_{45}Mn_{37}In_{13}Co_5$ ribbons, etc., and was ascribed to small angle grain boundaries [30-32]. In addition, within some grains, the martensite showed a single-variant domain structure. The above two characteristics of martensite morphologies seem to enhance the mobility of phase boundary, which is favorable for the reverse transformation under a relatively low magnetic field. Fig. 2(b) is a TEM micrograph showing the twinned martensite with straight and clear interfaces. The corresponding selected area electron diffraction (SAED) pattern (Fig. 2(c)) exhibited five extra superlattice spots between two primary spots, as pointed out by the arrows, indicating the formation of a six-layered modulated martensite also referred to as 6M martensite [33, 34]. Such a modulated structure is not the most common martensitic structure in Ni-Mn-Z alloys though it has been reported for Ni-Co-Mn-In [33] and Ni-Mn-In [34] alloys.

Fig. 3(a) shows the DSC curve of the $Ni_{40}Co_{10}Mn_{41}Sn_9$ ribbons. By applying the conventional tangent extrapolation method, the start and finish temperatures for the M → A transition were A_s = 403 K, and A_f = 417 K. The peak temperature, A_p, was 410 K. The start and finish temperatures for the A → M transition were M_s = 395 K, and M_f = 380 K. The peak temperature, M_p, was 389 K. Upon both heating and cooling, a small step corresponding to the paramagnetic-ferromagnetic transition occurred at around 440 K corresponding to the Curie temperature of austenite (T_C^A). Since the A_s temperature was as high as 403 K, a high temperature magnetic-field-induced reverse transformation is expected. The transformation entropy change (ΔS_{tr}) was calculated using the equation $\Delta S_{tr} = \Delta E_{tr} / T_0$ [35], where T_0 is the equilibrium temperature ($T_0 = (A_f + M_s)/2$, namely 406 K) and ΔE_{tr} is the transformation enthalpy (19.1×10^3 J kg^{-1} for the M → A transition

and 17.9×10^3 J kg^{-1} for the A → M transition, respectively), both of which have been determined from the DSC curves. Accordingly, ΔS_{tr}^{H} associated with the M → A transition and ΔS_{tr}^{C} associated with the A → M transition of the present ribbons were 47.0 and -44.1 J kg^{-1} K^{-1}, respectively. The absolute value of ΔS_{tr}^{H} was a little larger than that of ΔS_{tr}^{C}. According to the model proposed by Pecharsky et al. [36] and confirmed by Recarte et al. [37], that the maximum $\Delta S_M \approx \Delta S_{tr}$ provided that the applied field induced the complete reverse transformation, extremely large ΔS_M would be expected in the present ribbons for both cooling and heating magneto-structural transitions.

Fig. 3(b) compares low-field (5 mT) and high-field (2 T) magnetization as a function of temperature, $M(T)$, curves measured in zero-field-cooling (ZFC) and field-cooling (FC) modes between 310 and 550 K. The inset shows the dM/dT vs. T curve at 5 mT field, from which A_p and M_p were determined for the M → A (404 K) and A → M transitions (385 K). T_C^A was 433 K. All these characteristic temperatures were very close to those measured by DSC in Fig. 3(a). Small discrepancies are attributed to instruments error and different scanning rates as well as that indeed both techniques measure different physical magnitudes. As expected, both Fig. 3 (a) and (b) indicate that the microstructure was fully martensite at room temperature (293 K), which agrees well with the SEM and TEM results.

By applying a magnetic field of 2 T, the structural phase transformations were shifted towards lower temperature and the magnetization increased remarkably. A_p and M_p dropped by 6 and 5 K to 398 and 380 K, respectively, showing the distinct dependence of transformation temperatures on the external magnetic field. This is due to the magnetic field induced reverse martensitic transformation, a common feature for Ni-Mn-Z (Z=In, Sn and Sb) metamagnetic shape memory alloys. The ratio between transformation temperature change and magnetic field change ($\Delta T/\mu_o \Delta H$) was 3 K/T when referring to A_p. This ratio is smaller than that of some

reported Ni-Mn-Z alloys such as $Ni_{45}Co_5Mn_{36.6}In_{13.4}$ [38] and $Ni_{43}Co_7Mn_{39}Sn_{11}$ [39], in which $\Delta T/\mu_o\Delta H$ are 4.3 and 3.6 K/T, respectively. The reduced value for $Ni_{40}Co_{10}Mn_{41}Sn_9$ can be ascribed to extremely high value of ΔS_{tr}. According to the Clausius-Clapeyron relation [38], $\Delta T/\Delta\mu_o H = \Delta M_{A\text{-}M}/\Delta S_{tr}$ ($\Delta M_{A\text{-}M}$ is the difference in magnetization between the austenite and martensite phases). ΔS_{tr} associated with the M → A transition was 47.0 J kg^{-1} K^{-1} as obtained by DSC measurement. By using $\mu_o\Delta H$ = 2 T and $\Delta M_{A\text{-}M}$ = 67.6 Am^2 kg^{-1} as obtained in Fig. 3(b), $\Delta T/\mu_o\Delta H_{cal}$ (theoretical value) was 2.9 K/T, in accordance with the experimental value (3 K/T). Hence, in case of a similar $\Delta M_{A\text{-}M}$, a high value of ΔS_{tr} results in a small shift of ΔT, which limits the working temperature range of magnetic cooling materials. However, a high value of ΔS_{tr} also means a giant MCE effect. Therefore, we have to balance the maximum value and the width of the temperature range of the MCE to meet practical demand.

3.2 Magnetocaloric properties upon the reverse martensitic transformation.

Fig. 4(a) shows the isothermal magnetization versus magnetic field curves $M(\mu_o H)$ through the M → A transition. Similar to our previous results reported in Ref. [40], the curves can be divided into three groups including typical ferromagnetic behaviors with different magnitudes of maximum magnetization occurring at 5 T below 389 K and above 402 K, as well as a metamagnetic-like behavior between 389 K and 402 K. In Ni-Mn-Z Heusler alloys such metamagnetic-like behavior (i.e. the double-S shape of the *M-H* curve with a steep increase of magnetization over an intermediate magnetic field range) is believed to contribute substantially to ΔS_M^{peak} across the M → A transition [20].

We calculated the ΔS_M using the Maxwell relation (i.e., $\Delta S_M(T,\mu_0 H) = \mu_0 \int_0^{\mu_0 H} \left[\frac{\partial M(T,\mu_0 H')}{\partial T}\right]_{\mu_0 H'} dH'$) and plotted its dependence on the temperature ($\Delta S_M(T)$ curve) and magnetic field change in Fig. 4(b). In agreement with the sharp magnetization change,

the $\Delta S_M(T)$ curves show narrow peaks similar to those reported for other Ni-Mn-Z alloys exhibiting giant magnetocaloric effect [12, 13, 16, 41, 42]. These peaks occurred above 390 K indicating that the working temperature far exceeds room temperature, which is much higher than most of Ni-Mn-Z magnetic refrigerants. The peak position shifted to lower temperatures upon increasing $\mu_o\Delta H$ (as indicated in the figure by the dashed curved arrow). This shift resulted from the magnetic-field-induced shift of the phase transition temperatures. The maximum entropy change ΔS_M^{peak} first increased and then saturated with increasing magnetic field as shown in the inset of Fig. 4(b). For $\mu_o\Delta H$ = 5 T, the ΔS_M^{peak} reached 33.9 J kg^{-1} K^{-1} which is among the largest magnetic entropy changes reported for Ni-Mn-Z alloys, such as $Ni_{45}Mn_{37}In_{13}Co_5$ ribbon (ΔS_M^{peak} = 34 J kg^{-1} K^{-1}) [17], $Ni_{50}Mn_{34.5}In_{12.5}Ga_3$ (ΔS_M^{peak} = 36 J kg^{-1} K^{-1}) [43], $Ni_{46}Co_4Mn_{38}Sb_{12}$ (ΔS_M^{peak} = 29 J kg^{-1} K^{-1}) [16], $Ni_{50}Mn_{35.3}In_{14.7}$ (ΔS_M^{peak} = 28.6 J kg^{-1} K^{-1}) [44], $Ni_{45}Co_5Mn_{36.6}In_{13.4}$ (ΔS_M^{peak} = 28.4 J kg^{-1} K^{-1}) [38], and $Ni_{45}(Co_{0.95}Fe_{0.05})_5Mn_{36.6}In_{13.4}$ (ΔS_M^{peak} = 26 J kg^{-1} K^{-1}) [45]. Even for a much lower magnetic field change of 2 T, the ΔS_M^{peak} was 25 J kg^{-1} K^{-1}, still a considerable MCE. A summary of the magnetocaloric properties derived from the entropy change curves for five selected field change values is given in Table I.

To evaluate the working temperature range, we use δT_{FWHM}, the full-width at half-maximum of the $\Delta S_M(T)$ curve, i.e., $\delta T_{FWHM} = T_{hot} - T_{cold}$ where T_{hot} and T_{cold} are the temperatures at which ΔS_M is half the maximum value. The field dependence of the temperatures T_{hot} and T_{cold} is shown in the inset of Fig. 4(c) and the detailed values of δT_{FWHM}, T_{hot} and T_{cold} are listed in Table I. T_{cold} exhibited a stronger temperature dependence (decreasing from 399 to 391 K) than T_{hot} (decreasing from 402 to 400 K) with increasing the field to 5 T. Under 5 T field, δT_{FWHM} was only 9 K. As mentioned above, such a narrow working temperature range results from the abrupt magnetization change.

Refrigerant capacity *RC*, a physical quantity that quantifies the amount of heat that might be transferred between the cold and the hot reservoir through an ideal refrigeration cycle, is another important parameter that characterizes magnetocaloric materials [1, 46, 47]. The value of *RC* depends on $|\Delta S_M^{peak}|$ and on the temperature width of the ΔS_M curve [48]. From the practical viewpoint, three different criteria have been defined to estimate *RC* from the $\Delta S_M(T)$ curve [1, 46, 47]: (a) by the product $|\Delta S_M^{peak}| \times \delta T_{FWHM}$ (usually referred to as *RC*-1); (b) by the integral under the $\Delta S_M(T)$ curve between T_{hot} and T_{cold} (referred to as *RC*-2); and (c) by the maximum of the product $|\Delta S_M^{peak}| \times \delta T$ below the $\Delta S_M(T)$ curve (referred to as *RC*-3). The dependence of *RC*-1, *RC*-2, and *RC*-3 on $\mu_o \Delta H$ is depicted in Fig. 4(c) and the obtained values are listed in Table I. *RC*-1, *RC*-2, and *RC*-3 increased monotonically with increasing magnetic field change. For $\mu_o \Delta H$ = 5 T, the *RC*-1 value (294 J kg^{-1}) attained not considering the hysteresis losses is smaller than that in $Ni_{40}Co_{10}Mn_{40}Sn_{10}$ (426 J kg^{-1}) which has heretofore the largest *RC* reported in Ni-Mn-Z Heusler alloys [49]. However, the present *RC*-1 is higher than other Ni-Mn-Sn alloys (*RC*-1 = 80 J kg^{-1} for $Ni_{50}Mn_{36}Sn_{14}$ [42], 202 J kg^{-1} for $Ni_{44}Fe_2Mn_{43}Sn_{11}$ [50], and about 220 J kg^{-1} for $Ni_{43}Mn_{46}Sn_{11}C_2$ [51]). All these *RC*-1 values were obtained under a magnetic field change of 5 T. According to the definition of *RC*-1, extremely large value of ΔS_M^{peak} (33.9 J kg^{-1} K^{-1}) makes greater contributions to achieve such a large *RC*-1, compared with the role of δT_{FWHM} (9 K).

For Ni-Mn-Z magnetic cooling materials, the magnetic hysteresis losses originating from the field-induced reverse martensitic transformation are inevitable and must be subtracted from the obtained *RC* value to obtain an effective value, RC_{eff}. The hysteresis losses were estimated up to a maximum applied magnetic field of 2 T from the set of field-up and field-down isothermal $M(\mu_o H)$ curves shown in Fig. 5(a) (the value of 2 T was chosen because it is usually assumed as the maximum reference field change value with technological relevance). Fig. 5(b) displays the hysteresis loss dependence on the temperature at $\mu_o \Delta H$ = 2 T. For the studied alloy, the average

hysteresis loss, <*HL*> was up to 24.8 J kg^{-1}. Thus, by subtracting <*HL*> from the corresponding *RC* value at 2 T (i.e., 96 J kg^{-1}), RC_{eff} is 71.2 J kg^{-1}. That is, across the M → A transition, 25% reduction of refrigerant capacity will take place through an ideal refrigeration cycle. The present RC_{eff} is still higher than that of other Ni-Mn-Z alloys such as $Ni_{49}Mn_{39}Sn_{12}$ (58 J kg^{-1}) [52].

3.3 Magnetocaloric properties upon the forward martensitic transformation.

Fig. 6(a) shows the $M(\mu_o H)$ curves through the A → M transition. They differ in two aspects in comparison with those measured across the M → A transition (Fig.4 (a)). First, up to 4 T, isothermal magnetization curves show a low positive slope reflecting a weak magnetic field induced transition; however, above this threshold field a more pronounced field-induced metamagnetic-like behaviour appears. Liu et al. [20] suggested that the absence of magnetic field-induced reverse martensitic transformation contradicts a giant MCE for Ni-Mn-Z Heusler alloys, but this is not the case here. Second, the maximum magnetization upon cooling under 5 T reached 78.5 A m^2 kg^{-1}, a little higher than that across the M → A transition (76.5 A m^2 kg^{-1}).

$\Delta S_M(T)$ curves and the dependence of the absolute value of ΔS_M^{peak} on magnetic field change are plotted in Fig. 6(b). Similar to those measured for the M → A transition (Fig. 4(b)), all $\Delta S_M(T)$ curves show a narrow peak above 390 K. The difference is that, the peak position keeps constant upon increasing $\mu_o \Delta H$ (as indicated in the figure by the vertical dashed arrow). This further confirms that through the A → M transition the effect of the magnetic field on the magneto-structural transition is different compared to the metamagnetic-like behaviour occurring across the M → A transition. $|\Delta S_M^{peak}|$ increased linearly with $\mu_o \Delta H$ as shown in the inset of Fig. 6(b), in contrast with the saturating trend observed across the M → A transition (shown in the inset of Fig. 4(b)). For $\mu_o \Delta H$ = 5 T, $|\Delta S_M^{peak}|$ reached 53.3 J kg^{-1} K^{-1} which is 19.4 J kg^{-1} K^{-1} larger than that obtained across the M → A transition. Under 2 T field, $|\Delta S_M^{peak}|$ was 21.4 J kg^{-1} K^{-1}, just a little smaller than that (25 J kg^{-1} K^{-1}) obtained across the M → A transition. A summary of

the magnetocaloric properties derived from the $\Delta S_M(T)$ curves for five selected field change values is given in Table Ⅱ.

The field dependence of the temperatures T_{hot} and T_{cold} is shown in the inset of Fig. 6(c) and the specific values of δT_{FWHM}, T_{hot} and T_{cold} are listed in Table Ⅱ. Both T_{cold} and T_{hot} were almost independent of the magnetic field change and maintained stable values of ~388.5 and ~393 K, respectively, leading to a constant width of δT_{FWHM} (δT_{FWHM} = 4.4 and 4.7 K for 1 and 5 T field, respectively). The latter was similar to that measured at 2 T but about half of the value measured for the M → A transition at 5 T (δT_{FWHM} was 9 K under 5 T field). The absence of magnetic field induced structural transition upon cooling as indicated in Fig. 6(a) may cause a narrower working temperature range.

The dependence of *RC*-1, *RC*-2, and *RC*-3 on $\mu_o\Delta H$ is depicted in Fig. 6(c) and the explicit values are given in Table Ⅱ. *RC*-1, *RC*-2, and *RC*-3 increased monotonically with increasing magnetic field change, showing a similar trend as for the M → A transition. For $\mu_o\Delta H$ = 5 T, the *RC*-1 value (253 J kg^{-1}) was smaller than that produced by the M → A transition (294 J kg^{-1}), which can be ascribed to a much smaller value of δT_{FWHM} for the A → M transition that overcompensates the slightly larger ΔS_M^{peak}.

$|\Delta S_M^{peak}|$ vs. $\mu_o\Delta H$ curves are compared in Fig. 7. For the M → A transition, with increasing the magnetic field, $|\Delta S_M^{peak}|$ initially increased quickly and saturated above about 4 T. For the A → M transition, with increasing the magnetic field, $|\Delta S_M^{peak}|$ increased linearly up to 5 T. At $\mu_o\Delta H \approx 2.7$ T, the same $|\Delta S_M^{peak}|$ of 29.3 J kg^{-1} K^{-1} was attained for both transformations. Below 2.7 T field, $|\Delta S_M^{peak}|$ of the M → A was larger than that of A → M transition. Above 2.7 T field, it was the opposite. We consider that for Ni-Mn-Z (Z = In, Sn, Sb) alloys, ΔS_M is the sum of two components $\Delta S_{M,\ meta}$ and $\Delta S_{M,\ therm}$ representing the ΔS_M contributions from the field-induced metamagnetic-like magnetization behaviour and thermally induced magnetization behaviour,

respectively. As confirmed in Fig. 4(a) and Fig. 6(a), below 2.7 T field, no metamagnetic-like magnetization behaviour occurred during the A → M transition leading to the absence of $\Delta S_{M,meta}$, while for the M → A transition, distinct metamagnetic-like magnetization behaviour results in a large $\Delta S_{M,\,meta}$. Thus, in case of similar $\Delta S_{M,\,therm}$, $|\Delta S_M^{peak}|$ for the A → M transition was smaller than that of the M → A transition. Above 2.7 T field, a considerable fraction of martensite had transformed to the austenite induced by the applied field, so the role of $\Delta S_{M,\,meta}$ decreased and the contribution of $\Delta S_{M,\,therm}$ increased. Isothermal magnetization curves under high field in Fig.4 (a) and Fig. 6 (a) clearly showed that, the magnetization change within a constant temperature interval ($\Delta M/\Delta T$) caused by the same magnetic field is different. The magnitude of $\Delta M/\Delta T$ for the A → M transition is much larger than that of the M → A transition, which would produce a higher magnetic entropy change according to the Maxwell relation. Consequently, above 2.7 T field, $|\Delta S_M^{peak}|$ for the M → A was smaller than that of the A → M transition.

Fig. 8(a) shows the field-up and field-down isothermal $M(\mu_o H)$ curves up to a maximum applied magnetic field of 2 T for temperatures between 386 and 398 K. The isothermal magnetization curves are almost completely reversible. The hysteresis loss values at different temperatures were determined by calculating the areas enclosed by the field-up and field-down $M(\mu_o H)$ curves and are shown in Fig. 8(b). The average hysteresis loss <*HL*> is as low as 0.36 J kg^{-1}, which is only 1.5% of that (24.8 J kg^{-1}) of the M → A transition and also far below the values reported for several Ni-Mn-Z (Z = In, Sn, Sb) alloys. For example, 8.3 J kg^{-1} (2 T) for $Ni_{50.3}Mn_{35.5}Sn_{14.4}$ ribbon [53], 19 J kg^{-1} (2 T) for $Ni_{40.6}Co_{8.5}Mn_{40.9}Sn_{10}$ unidirectional crystal [40], 2.2 J kg^{-1} (2 T) for $Ni_{50}Mn_{34}In_{16}$ polycrystal [54], 3.46 J kg^{-1} (1.5 T) for $Ni_{47.5}Mn_{37.5}Sn_{15}$ polycrystal [55], 11 J kg^{-1} (3 T) for $Mn_{50}Ni_{40}In_{10}$ ribbon [56], 13.0 J kg^{-1} (5 T) for $Ni_{50}Mn_{37}Sb_{13}$ polycrystal [15], 14 J kg^{-1} (5 T) for $Ni_{41}Co_9Mn_{40}Sb_{10}$ polycrystal [57], 57 J kg^{-1} (7 T) for $Ni_{45}Co_5Mn_{37.5}In_{12.5}$ single crystal [58]. In these cases, the values in parentheses represent the

applied magnetic field. Upon heating, the magnetic field induces the M → A transition leading to large hysteretic losses [53]. Thus, low loss upon cooling can be ascribed to the lack of the magnetic field-induced A → M transition. By subtracting the <*HL*> from the corresponding *RC* value at 2 T (i.e., 96 J kg^{-1}), RC_{eff} is 95.6 J kg^{-1} which is much larger than that produced by the M → A transition (71.2 J kg^{-1}). Through an ideal refrigeration cycle associated with the M → A transition, magnetic hysteresis loss has been a major problem since it significantly decreases the cooling efficiency [59].

3.4 Comparison with Ni-Mn-Z magnetocaloric alloys.

For comparison, the values of $|\Delta S_M^{peak}|$ for the present sample, most studied Ni-Mn-Z magnetocaloric alloys, $Gd_5Ge_2Si_2$, La(Fe, Si)$_{13}$-based alloys, and (Mn,Fe)$_2$P-type compounds are schematically illustrated in Fig. 9. The peak temperature of $\Delta S_M(T)$ curves of those materials is limited to be around or above room temperature. We make two major observations. First, the temperature (391 and 396 K) at which a large $|\Delta S_M^{peak}|$ appears for the presently fabricated ribbons is much higher than for any other materials reported except our previously $Ni_{37.7}Co_{12.7}Mn_{40.8}Sn_{8.8}$ ribbon [22]. Even more importantly, the $|\Delta S_M^{peak}|$ upon cooling is the largest for Ni-Mn-Z (Z=In, Sn, Sb) Heusler alloys reported so far. Also, a small hysteresis loss greatly enhances the cooling efficiency. The present findings open up the possibility of elevated temperature magnetic cooling with high efficiency.

4. CONCLUSIONS

In summary, we demonstrated a magnetostructural transition clearly above 100 °C for $Ni_{40}Co_{10}Mn_{41}Sn_9$ ribbon. Giant magnetic entropy change is achieved not only upon heating (the M → A transition) but also upon cooling (the A → M transition). Particularly for the latter, an extremely large $|\Delta S_M^{peak}|$ value of 53 J kg^{-1} K^{-1} (ascribed to the great transformation entropy change) along with a negligible hysteresis loss (on average only 0.36 J kg^{-1}, due to the

disappearance of the magnetic field-induced structural transition) was discovered. As compared to other Ni-Mn-Z magnetic refrigerant materials reported to date, the present $|\Delta S_M^{peak}|$ is the largest while the hysteresis loss is the smallest. The present work demonstrates a possible way to develop a high-temperature, high efficiency magnetic cooling technique.

ACKNOWLEDGEMENTS

The National Natural Science Foundation of China (51101040), the Fundamental Research Funds for the Central Universities (HEUCF171007), and the State Scholarship Fund of China supported this work. PM acknowledges financial support through the National Science Foundation through grant No DMR-1207192. J.L. Sánchez Llamazares acknowledges the scientific and financial support received from Laboratorio Nacional de Investigaciones en Nanociencias y Nanotecnología (LINAN, IPICyT). C.F. Sánchez-Valdés is grateful to DMCU-UACJ for supporting his 2017 summer research stay at IPICyT (program PFCE and academic mobility grant).

REFERENCES

[1] A.M. Tishin, Y.I. Spichkin, The magnetocaloric effect and its applications, Institute of Physics Publishing, Bristol, 2003.
[2] R. Kumar, Mater. Today 4 (2017) 5544-5551.
[3] V. Franco, J.S. Blázquez, J.J. Ipus, J.Y. Law, L.M. Moreno-Ramírez, A. Conde, Prog. Mater. Sci. 93 (2018) 112-232.
[4] V.K. Pecharsky, K.A. Gschneidner Jr., Phys. Rev. Lett. 78 (1997) 4494-4497.
[5] V.K. Pecharsky, A.P. Holm, K.A. Gschneidner Jr., R. Rink, Phys. Rev. Lett. 91 (2003) 197204.
[6] C. Zimm, A. Jastrab, A. Sternberg, V. Pecharsky, K. Gschneidner, M. Osborne, I. Anderson, Description and Performance of a Near-Room Temperature Magnetic Refrigerator, in: P. Kittel (Ed.) Advances in Cryogenic Engineering, Springer US, 1998.
[7] J. Lyubina, J. Phys. D: Appl. Phys. 50 (2017) 053002.
[8] E. Brück, H. Yibole, L. Zhang, Philos. Trans. A 374 (2016).
[9] T. Krenke, E. Duman, M. Acet, E.F. Wassermann, X. Moya, L. Mañosa, A. Planes, Nat. Mater. 4 (2005) 450-454.
[10] I. Babita, S.I. Patil, S. Ram, J. Phys. D: Appl. Phys. 43 (2010) 205002.
[11] V.V. Khovaylo, K.P. Skokov, O. Gutfleisch, H. Miki, T. Takagi, T. Kanomata, V.V. Koledov, V.G. Shavrov, G. Wang, E. Palacios, J. Bartolomé, R. Burriel, Phys. Rev. B 81 (2010) 214406.
[12] T. Krenke, E. Duman, M. Acet, X. Moya, L. Mañosa, A. Planes, J. Appl. Phys. 102 (2007) 033903.
[13] Z.D. Han, D.H. Wang, B. Qian, J.F. Feng, X.F. Jiang, Y.W. Du, Jpn. J. Appl. Phys. 49 (2010) 010211.
[14] J. Du, Q. Zheng, W.J. Ren, W.J. Feng, X.G. Liu, Z.D. Zhang, J. Phys. D: Appl. Phys. 40 (2007) 5523-5526.
[15] M. Khan, N. Ali, S. Stadler, J. Appl. Phys. 101 (2007) 053919.
[16] A.K. Nayak, K.G. Suresh, A.K. Nigam, J. Phys. D: Appl. Phys. 42 (2008) 035009.
[17] J. Liu, N. Scheerbaum, J. Lyubina, O. Gutfleisch, Appl. Phys. Lett. 93 (2008) 102512.
[18] L. Mañosa, D. González-Alonso, A. Planes, E. Bonnot, M. Barrio, J.L. Tamarit, S. Aksoy, M. Acet, Nat. Mater. 9 (2010) 478-481.
[19] V.K. Sharma, M.K. Chattopadhyay, L.S. Sharath Chandra, S.B. Roy, J. Phys. D: Appl. Phys. 44 (2011) 145002.
[20] J. Liu, T. Gottschall, K.P. Skokov, J.D. Moore, O. Gutfleisch, Nat. Mater. 11 (2012) 620-626.
[21] S. Fabbrici, J. Kamarad, Z. Arnold, F. Casoli, A. Paoluzi, F. Bolzoni, R. Cabassi, M. Solzi, G. Porcari, C. Pernechele, Acta Mater. 59 (2011) 412-419.
[22] F. Chen, W.L. Liu, Y.G. Shi, P. Müllner, J. Magn. Magn. Mater. 377 (2015) 137-141.
[23] R. Kainuma, K. Oikawa, W. Ito, Y. Sutou, T. Kanomata, K. Ishida, J. Mater. Chem. 18 (2008) 1837.
[24] F. Chen, Y.X. Tong, B. Tian, Y.F. Zheng, Y. Liu, Intermetallics 18 (2010) 188-192.
[25] F. Chen, Y.X. Tong, B. Tian, L. Li, Y.F. Zheng, Mater. Lett. 64 (2010) 1879-1882.
[26] F. Chen, Y.X. Tong, B. Tian, L. Li, Y.F. Zheng, Y. Liu, J. Magn. Magn. Mater. 347 (2013) 72-74.
[27] O. Gutfleisch, A. Yan, K.H. Müller, J. Appl. Phys. 97 (2005) 10M305.
[28] A. Quintana-Nedelcos, J.L. Sánchez Llamazares, C.F. Sánchez-Valdés, P. Álvarez Alonso, P. Gorria, P. Shamba, N.A. Morley, J. Alloys Compd. 694 (2017) 1189-1195.

[29] F. Chen, Y.X. Tong, Y.J. Huang, B. Tian, L. Li, Y.F. Zheng, Intermetallics 36 (2013) 81-85.
[30] J. Liu, T.G. Woodcock, N. Scheerbaum, O. Gutfleisch, Acta Mater. 57 (2009) 4911-4920.
[31] S.C. Ma, Q.Q. Cao, H.C. Xuan, C.L. Zhang, L.J. Shen, D.H. Wang, Y.W. Du, J. Alloys Compd. 509 (2011) 1111-1114.
[32] S.C. Ma, C.W. Shih, J. Liu, J.H. Yuan, S.Y. Lee, Y.I. Lee, H.W. Chang, W.C. Chang, Acta Mater. 90 (2015) 292-302.
[33] W. Ito, M. Nagasako, R.Y. Umetsu, R. Kainuma, T. Kanomata, K. Ishida, Appl. Phys. Lett. 93 (2008) 232503.
[34] H. Yan, Y. Zhang, N. Xu, A. Senyshyn, H.-G. Brokmeier, C. Esling, X. Zhao, L. Zuo, Acta Mater. 88 (2015) 375-388.
[35] P. Wollants, J.R. Roos, L. Delaey, Prog. Mater. Sci. 37 (1993) 227-288.
[36] V. Pecharsky, K. Gschneidner, A. Pecharsky, A. Tishin, Phys. Rev. B 64 (2001).
[37] V. Recarte, J.I. Pérez-Landazábal, S. Kustov, E. Cesari, J. Appl. Phys. 107 (2010) 053501.
[38] R. Kainuma, Y. Imano, W. Ito, Y. Sutou, H. Morito, S. Okamoto, O. Kitakami, K. Oikawa, A. Fujita, T. Kanomata, K. Ishida, Nature 439 (2006) 957-960.
[39] R. Kainuma, Y. Imano, W. Ito, H. Morito, Y. Sutou, K. Oikawa, A. Fujita, K. Ishida, S. Okamoto, O. Kitakami, T. Kanomata, Appl. Phys. Lett. 88 (2006) 192513.
[40] F.Chen, Y. X.Tong, L.Li, J. L.Sánchez Llamazares, C. F.Sánchez-Valdés, P.Müllner, J. Alloys Compd. 691 (2017) 269-274.
[41] S. Aksoy, T. Krenke, M. Acet, E.F. Wassermann, X. Moya, L. Mañosa, A. Planes, Appl. Phys. Lett. 91 (2007) 241916.
[42] T.L. Phan, P. Zhang, N.H. Dan, N.H. Yen, P.T. Thanh, T.D. Thanh, M.H. Phan, S.C. Yu, Appl. Phys. Lett. 101 (2012) 212403.
[43] A.Y. Takeuchi, C.E. Guimarães, E.C. Passamani, C. Larica, J. Appl. Phys. 111 (2012) 103902.
[44] X.X. Zhang, B. Zhang, S.Y. Yu, Z.H. Liu, W.J. Xu, G.D. Liu, J.L. Chen, Z.Z. Cao, G.H. Wu, Phys. Rev. B 76 (2007) 132403.
[45] L. Chen, F.X. Hu, J. Wang, L.F. Bao, J.R. Sun, B.G. Shen, J.H. Yin, L.Q. Pan, Appl. Phys. Lett. 101 (2012) 012401.
[46] K.A. Gschneidner Jr, V.K. Pecharsky, A.O. Pecharsky, C.B. Zimm, Mater. Sci. Forum 315-317 (1999) 69.
[47] M.E. Wood, W.H. Potter, Cryogenics 25 (1985) 667.
[48] C.F. Sánchez-Valdés, P.J. Ibarra-Gaytán, J.L.S. Llamazares, M. Ávalos-Borja, P. Álvarez-Alonso, P. Gorria, J.A. Blanco, Appl. Phys. Lett. 104 (2014) 212401.
[49] L. Huang, D.Y. Cong, H.L. Suo, Y.D. Wang, Appl. Phys. Lett. 104 (2014) 132407.
[50] X.G. Zhao, M. Tong, C.W. Shih, B. Li, W.C. Chang, W. Liu, Z.D. Zhang, J. Appl. Phys. 113 (2013) 17A913.
[51] Y. Zhang, J. Liu, Q. Zheng, J. Zhang, W.X. Xia, J. Du, A. Yan, Scr. Mater. 75 (2014) 26-29.
[52] J. Ren, H.W. Li, J.K. Yu, S.T. Feng, Q.J. Zhai, J.X. Fu, Z.P. Luo, H.X. Zheng, J. Alloys Compd. 634 (2015) 65-69.
[53] B. Hernando, J.L. Sánchez Llamazares, J.D. San

[58] D. Bourgault, J. Tillier, P. Courtois, D. Maillard, X. Chaud, Appl. Phys. Lett. 96 (2010) 132501.
[59] J. Shen, B. Gao, H.W. Zhang, F.X. Hu, Y.X. Li, J.R. Sun, B.G. Shen, Appl. Phys. Lett. 91 (2007) 142504.
[60] H. Wada, Y. Tanabe, Appl. Phys. Lett. 79 (2001) 3302.
[61] O. Tegus, E. Brück, K.H.J. Buschow, F.R. de Boer, Nature 415 (2002) 150.
[62] E. Brück, N.T. Trung, Z.Q. Ou, K.H.J. Buschow, Scr. Mater. 67 (2012) 590-593.
[63] C. Jing, J. P. Chen, Z. Li, S. X. Cao, J.C. Zhang, Acta Phys. Sin. 57 (2008) 4450-4455.
[64] J.L. Zhao, J. Shen, F.X. Hu, Y.X. Li, J.R. Sun, B.G. Shen, J. Appl. Phys. 107 (2010) 113911.
[65] J. Lyubina, K. Nenkov, L. Schultz, O. Gutfleisch, Phys. Rev. Lett. 101 (2008) 177203.
[66] J. Lyubina, O. Gutfleisch, M.D. Kuz'min, M. Richter, J. Magn. Magn. Mater. 321 (2009) 3571-3577.
[67] D.T. Cam Thanh, E. Brück, O. Tegus, J.C.P. Klaasse, K.H.J. Buschow, J. Magn. Magn. Mater. 310 (2007) e1012-e1014.
[68] A. Barcza, M. Katter, V. Zellmann, S. Russek, S. Jacobs, C. Zimm, IEEE Trans. Magn. 47 (2011) 3391-3394.
[69] F. Guillou, H. Yibole, N.H. van Dijk, L. Zhang, V. Hardy, E. Brück, J. Alloys Compd. 617 (2014) 569-574.
[70] A.K. Pathak, M. Khan, I. Dubenko, S. Stadler, N. Ali, Appl. Phys. Lett. 90 (2007) 262504.
[71] W.J. Feng, Q. Zhang, L.Q. Zhang, B. Li, J. Du, Y.F. Deng, Z.D. Zhang, Solid State Commun. 150 (2010) 949-952.
[72] A. Ghosh, K. Mandal, Appl. Phys. Lett. 104 (2014) 031905.
[73] J.L. Sánchez Llamazares, H. Flores-Zuñiga, C. Sánchez-Valdes, C.A. Ross, C. García, J. Appl. Phys. 111 (2012) 07A932.

Table I Magnetocaloric properties associated to the M → A structural transition under selected magnetic field changes. $\mu_o\Delta H$ is the applied magnetic field. $|\Delta S_M^{peak}|$ is the absolute value of the maximum magnetic entropy change. *RC*-1, *RC*-2, and *RC*-3 are three different criteria for estimating refrigerant capacity. T_{hot} and T_{cold} are the temperatures located at half-maximum of the $\Delta S_M(T)$ curve, the difference of which is δT_{FWHM}, the working temperature change. <*HL*> is the average hysteresis loss.

	M → A transition				
$\mu_o\Delta H$ (T)	1.0	2.0	3.0	4.0	5.0
$\|\Delta S_M^{peak}\|$ (J kg^{-1} K^{-1})	15.0	25.0	30.0	33.0	33.9
RC-1 (J kg^{-1})	44	96	159	226	294
RC-2 (J kg^{-1})	35	80	134	194	261
RC-3 (J kg^{-1})	22	50	86	130	182
<*HL*> (J kg^{-1})	-	24.8	-	-	-
δT_{FWHM} (K)	3	4	5	7	9
T_{hot} (K)	401	400	400	400	400
T_{cold} (K)	398	396	395	393	391

Table Ⅱ Magnetocaloric properties associated to the A → M structural transition under selected magnetic field changes. $\mu_o\Delta H$ is the applied magnetic field change. $|\Delta S_M^{peak}|$ is the absolute value of the maximum magnetic entropy change. *RC*-1, *RC*-2, and *RC*-3 are three different criteria for estimating refrigerant capacity. T_{hot} and T_{cold} are the temperatures located at half-maximum of the $\Delta S_M(T)$ curve, the difference of which is δT_{FWHM}, the working temperature change. <*HL*> is the average hysteresis loss.

A → M transition					
$\mu_o\Delta H$ (T)	1.0	2.0	3.0	4.0	5.0
$\|\Delta S_M^{peak}\|$ (J kg^{-1} K^{-1})	10.7	21.4	32.3	43.2	53.3
RC-1 (J kg^{-1})	47	96	146	198	253
RC-2 (J kg^{-1})	38	77	117	158	202
RC-3 (J kg^{-1})	24	48	74	100	128
<*HL*> (J kg^{-1})	-	0.36	-	-	-
δT_{FWHM} (K)	4.4	4.5	4.6	4.6	4.7
T_{hot} (K)	392.9	392.9	392.9	392.8	392.7
T_{cold} (K)	388.5	388.4	388.3	388.2	388.0

FIGURE CAPTIONS

Fig. 1. SEM image of the cross section of the ribbon.

Fig. 2. (a) SEM image, (b) TEM bright field image and (c) the corresponding selected area electron diffraction (SAED) pattern taken from the zone indicated in (b) by the dashed circle.

Fig. 3. (a) DSC curve of the ribbons. (b) Temperature dependence of magnetization under a static magnetic field of 5 mT and 2 T between 310 and 550 K. Inset: dM/dT vs. T curve at 5 mT field.

Fig. 4. (a) Isothermal magnetization curves obtained in the temperature range of 350-420 K. (b) $\Delta S_M(T)$ curves under magnetic field changes ranging from 1 to 5 T. Inset: ΔS_M^{peak} as a function of $\mu_o \Delta H$. (c) Refrigerant capacity (*RC*-1, *RC*-2, and *RC*-3) as a function of the magnetic field change. Inset: Field dependence of the temperatures T_{hot} and T_{cold} that define the $\delta T_{FWHM.}$.

Fig. 5. (a) Isothermal magnetization curves on increasing (field-up) and decreasing (field-down) the magnetic field. (b) Hysteresis loss across the M → A transition up to $\mu_o \Delta H_{max}$= 2 T.

Fig. 6. (a) Isothermal magnetization curves obtained in the temperature range of 373-395 K. (b) $\Delta S_M(T)$ curves under various magnetic field. Inset: ΔS_M^{peak} as a function of $\mu_o \Delta H$. (c) Refrigerant capacity (*RC*-1, *RC*-2, and *RC*-3) as a function of the magnetic field change. Inset: field dependence of the temperatures T_{hot} and T_{cold} that define the $\delta T_{FWHM.}$.

Fig. 7. The absolute value of ΔS_M^{peak} as a function of $\mu_o \Delta H$ for the M → A and A → M transitions.

Fig. 8. (a) Isothermal magnetization curves on increasing (field-up) and decreasing (field-down) the magnetic field. (b) Hysteresis loss across the A → M transition up to $\mu_o \Delta H_{max}$ = 2 T.

Fig. 9. $|\Delta S_M^{peak}|$ through the first-order structural transition around and above room temperature for Heusler alloys, $Gd_5Ge_2Si_2$, La(Fe, Si)$_{13}$-based alloys, and (Mn, Fe)$_2$P-type compounds [4, 9-20, 22, 38, 43-45, 49, 57, 58, 60-73]. The value of applied magnetic field change is distinguished by the filling color. For precise comparison, we select the data under a magnetic field of 5 T as far as possible. For sample 20, $|\Delta S_M^{peak}|$ is obtained upon cooling. Both samples 18 and 36 are $Ni_{50}Mn_{38}Sb_{12}$ but different results at different temperatures were reported by two laboratories. They are illustrated here together. Samples 33 and 34 are located at the same position in the figure. Note that the applied field for sample 33 is just 1 T, while 5 T for sample 34.

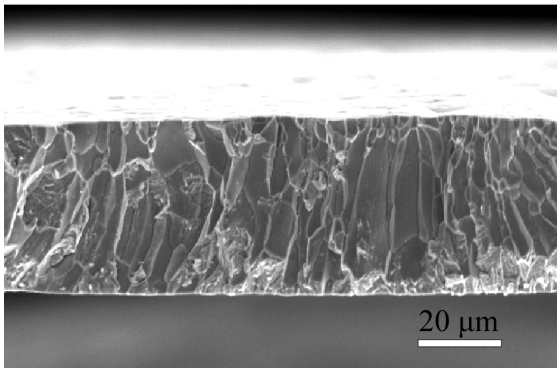

Fig. 1. SEM image of the cross section of the ribbon.

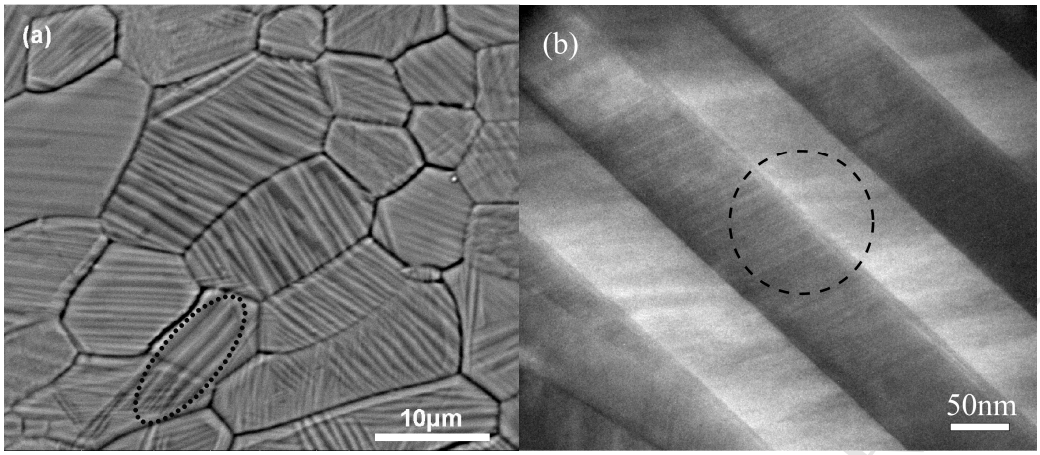

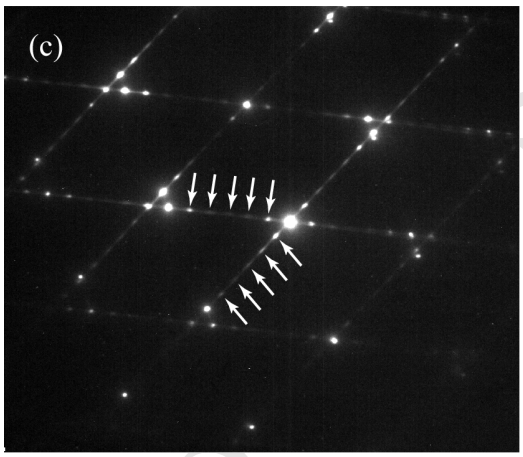

Fig. 2. (a) SEM image, (b) TEM bright field image and (c) the corresponding selected area electron diffraction (SAED) pattern taken from the zone indicated in (b) by the dashed circle.

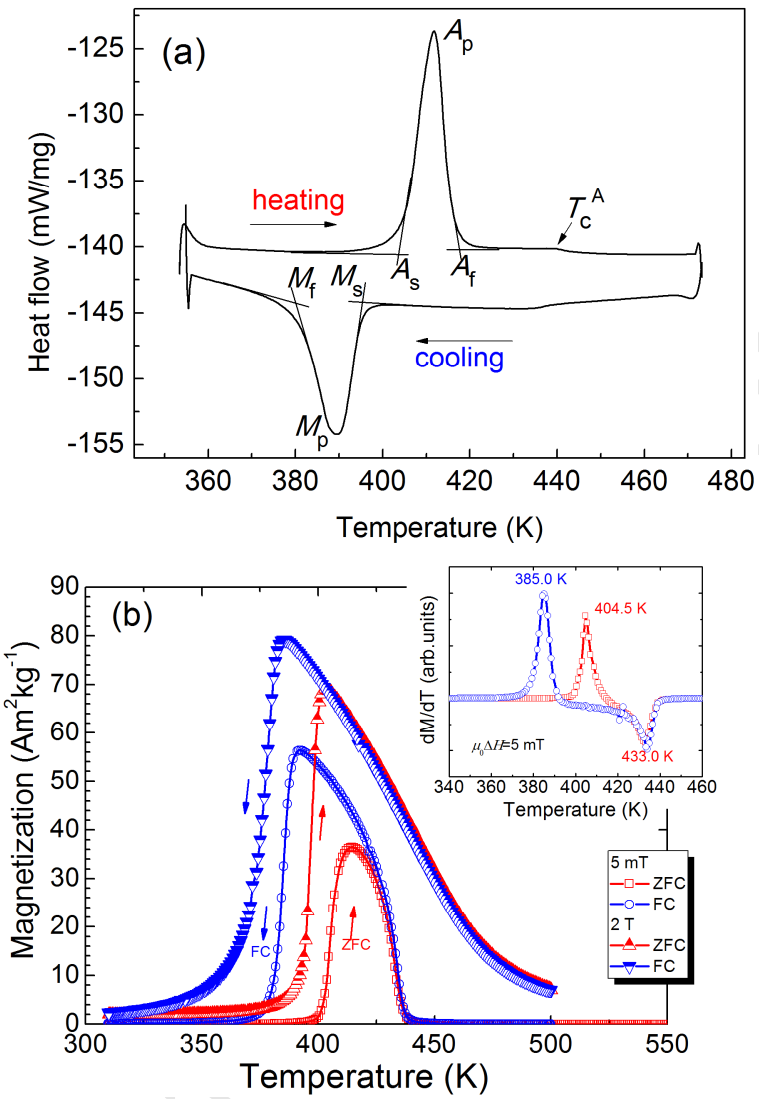

Fig. 3. (a) DSC curve of the ribbons. (b) Temperature dependence of magnetization under a static magnetic field of 5 mT and 2 T between 310 and 550 K. Inset: dM/dT vs. T curve at 5 mT field.

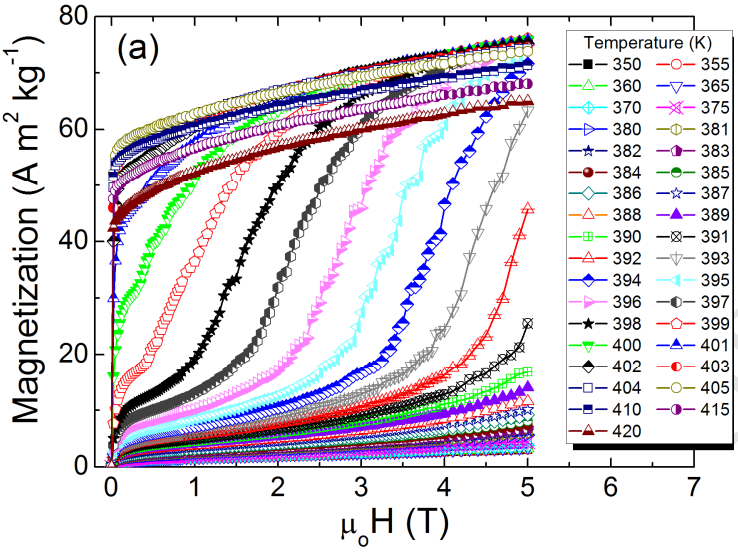
(a)
Magnetization (A m^2 kg^{-1})
μ_oH (T)
Temperature (K)
350 355
360 365
370 375
380 381
382 383
384 385
386 387
388 389
390 391
392 393
394 395
396 397
398 399
400 401
402 403
404 405
410 415
420

1

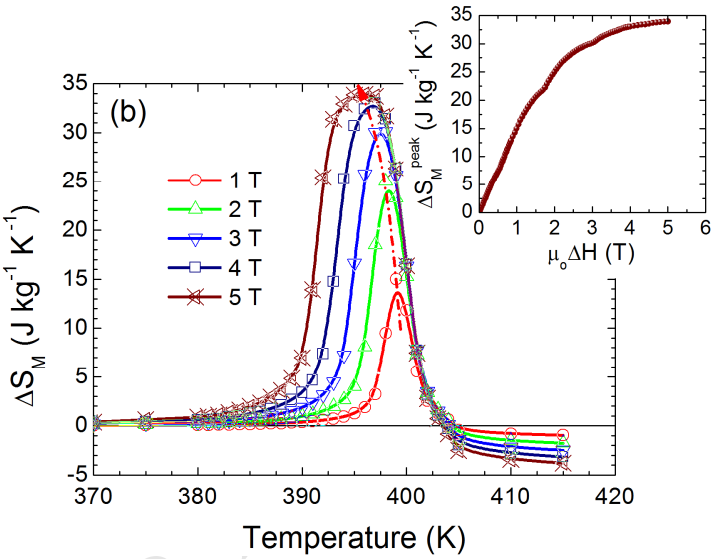
(b)
1 T
2 T
3 T
4 T
5 T
ΔS_M (J kg^{-1} K^{-1})
Temperature (K)
ΔS_M^{peak} (J kg^{-1} K^{-1})
$\mu_o\Delta H$ (T)

2

3

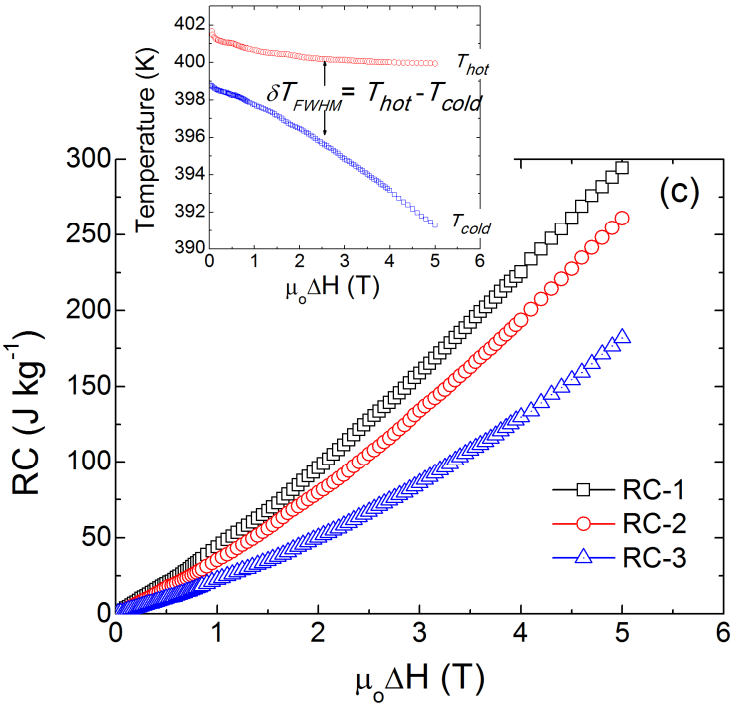

Fig. 4. (a) Isothermal magnetization curves obtained in the temperature range of 350-420 K. (b) $\Delta S_M(T)$ curves under magnetic field changes ranging from 1 to 5 T. Inset: ΔS_M^{peak} as a function of $\mu_o\Delta H$. (c) Refrigerant capacity (*RC*-1, *RC*-2, and *RC*-3) as a function of the magnetic field change. Inset: Field dependence of the temperatures T_{hot} and T_{cold} that define the δT_{FWHM}.

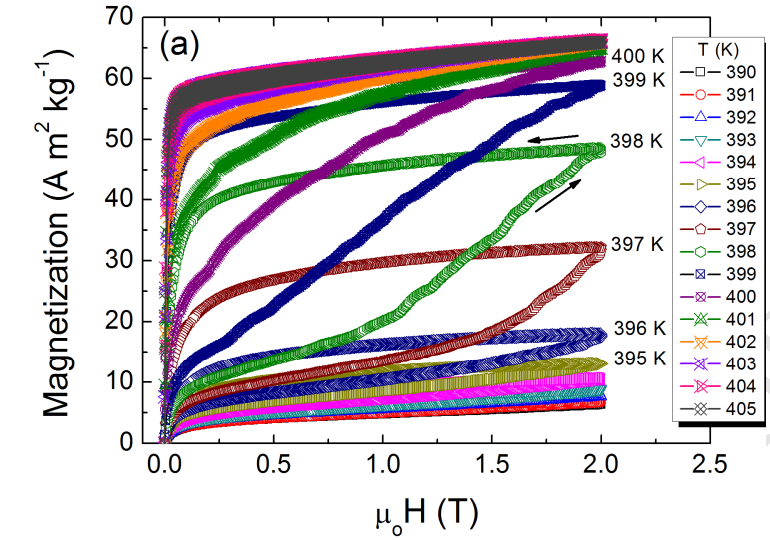

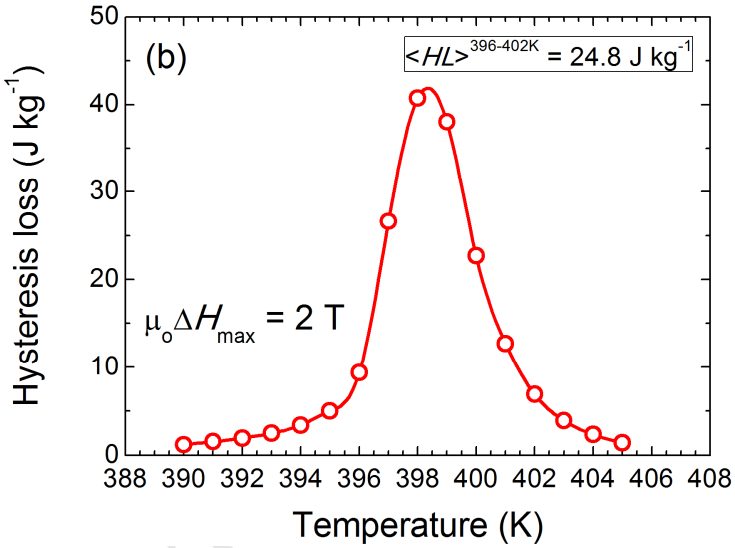

Fig. 5. (a) Isothermal magnetization curves on increasing (field-up) and decreasing (field-down) the magnetic field. (b) Hysteresis loss across the M → A transition up to $\mu_o\Delta H_{max}$= 2 T.

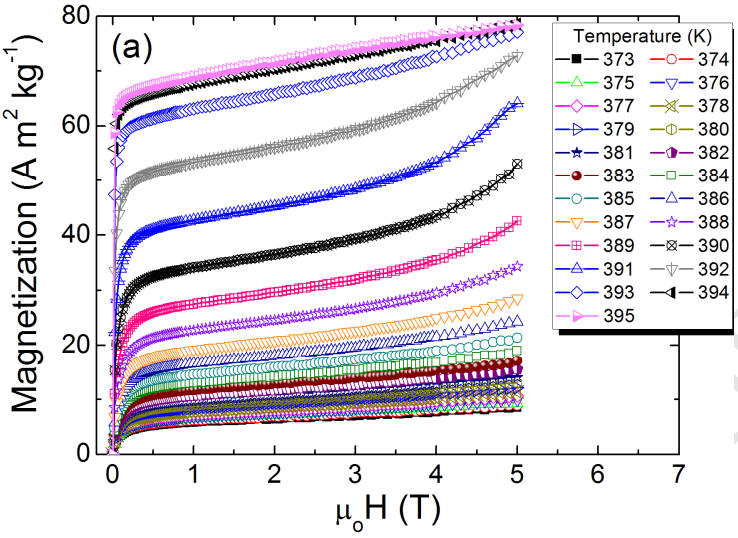
(a)
Magnetization (A m^2 kg^{-1})
μ_oH (T)
Temperature (K)
373
374
375
376
377
378
379
380
381
382
383
384
385
386
387
388
389
390
391
392
393
394
395

1

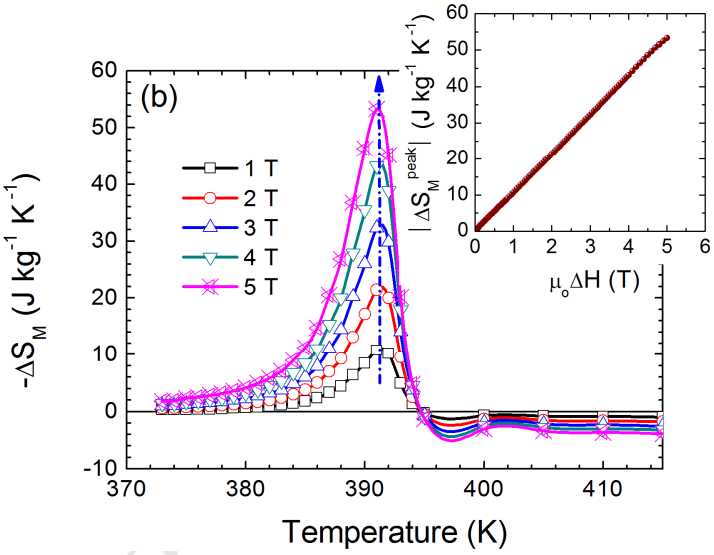
(b)
-ΔS_M (J kg^{-1} K^{-1})
Temperature (K)
1 T
2 T
3 T
4 T
5 T
$|\Delta S_M^{peak}|$ (J kg^{-1} K^{-1})
$\mu_o\Delta$H (T)

2

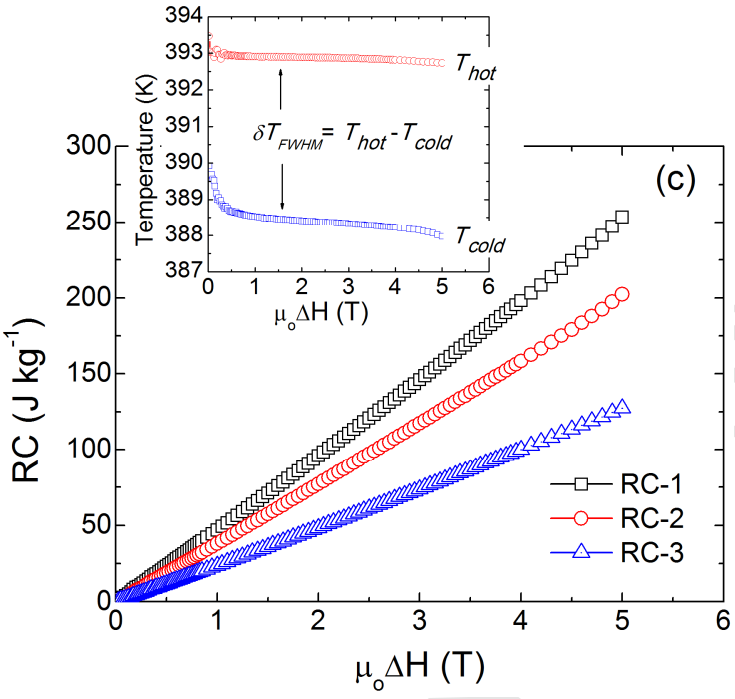

Fig. 6. (a) Isothermal magnetization curves obtained in the temperature range of 373-395 K. (b) $\Delta S_M(T)$ curves under various magnetic field. Inset: ΔS_M^{peak} as a function of $\mu_o\Delta H$. (c) Refrigerant capacity (*RC*-1, *RC*-2, and *RC*-3) as a function of the magnetic field change. Inset: field dependence of the temperatures T_{hot} and T_{cold} that define the δT_{FWHM}.

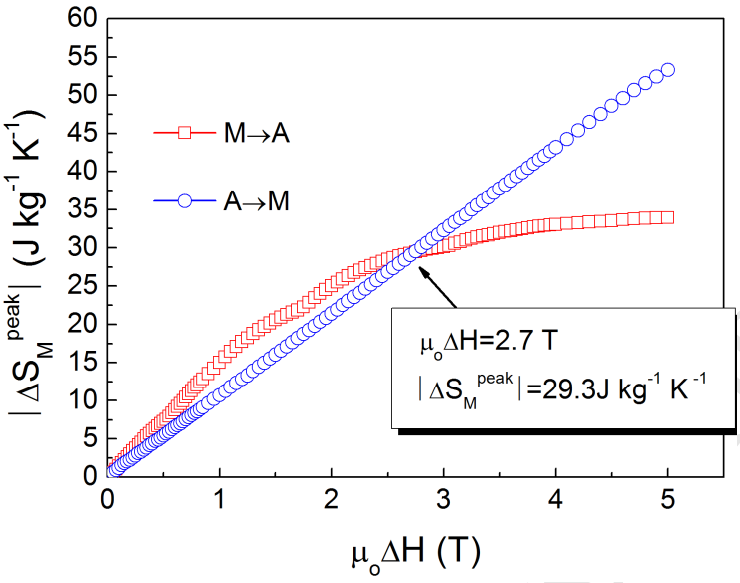

Fig. 7. The absolute value of ΔS_M^{peak} as a function of $\mu_o \Delta H$ for the M → A and A → M transitions.

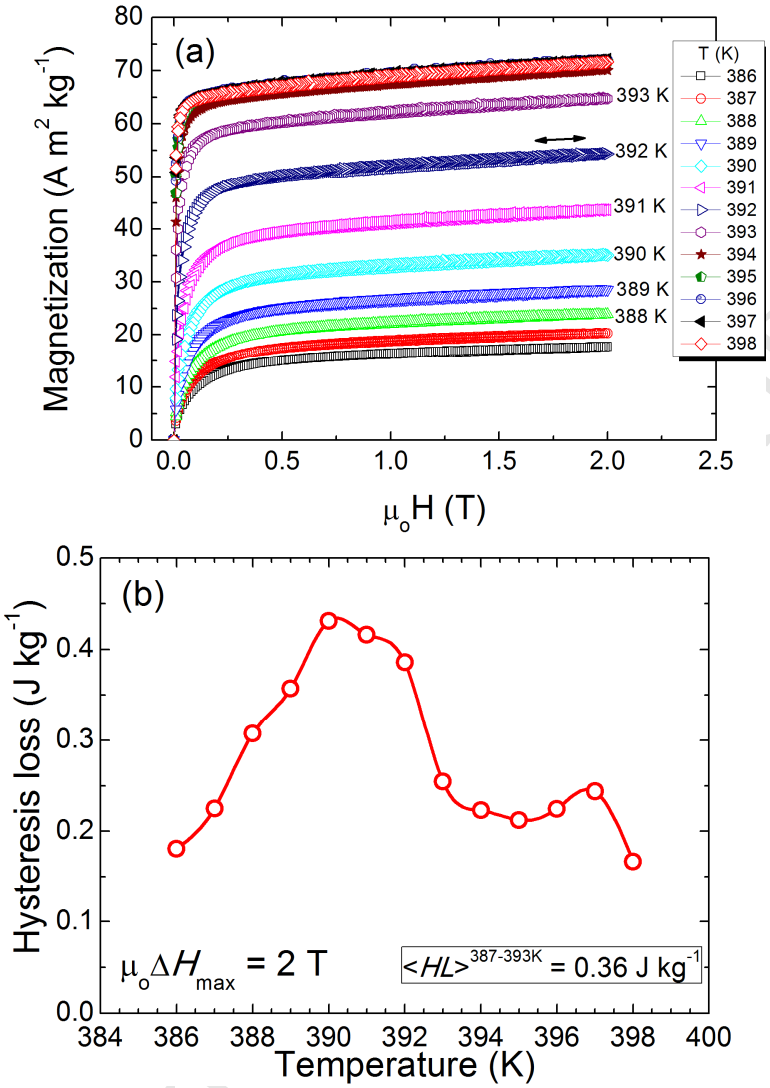

Fig. 8. (a) Isothermal magnetization curves on increasing (field-up) and decreasing (field-down) the magnetic field. (b) Hysteresis loss across the A → M transition up to $\mu_o \Delta H_{max}$ = 2 T.

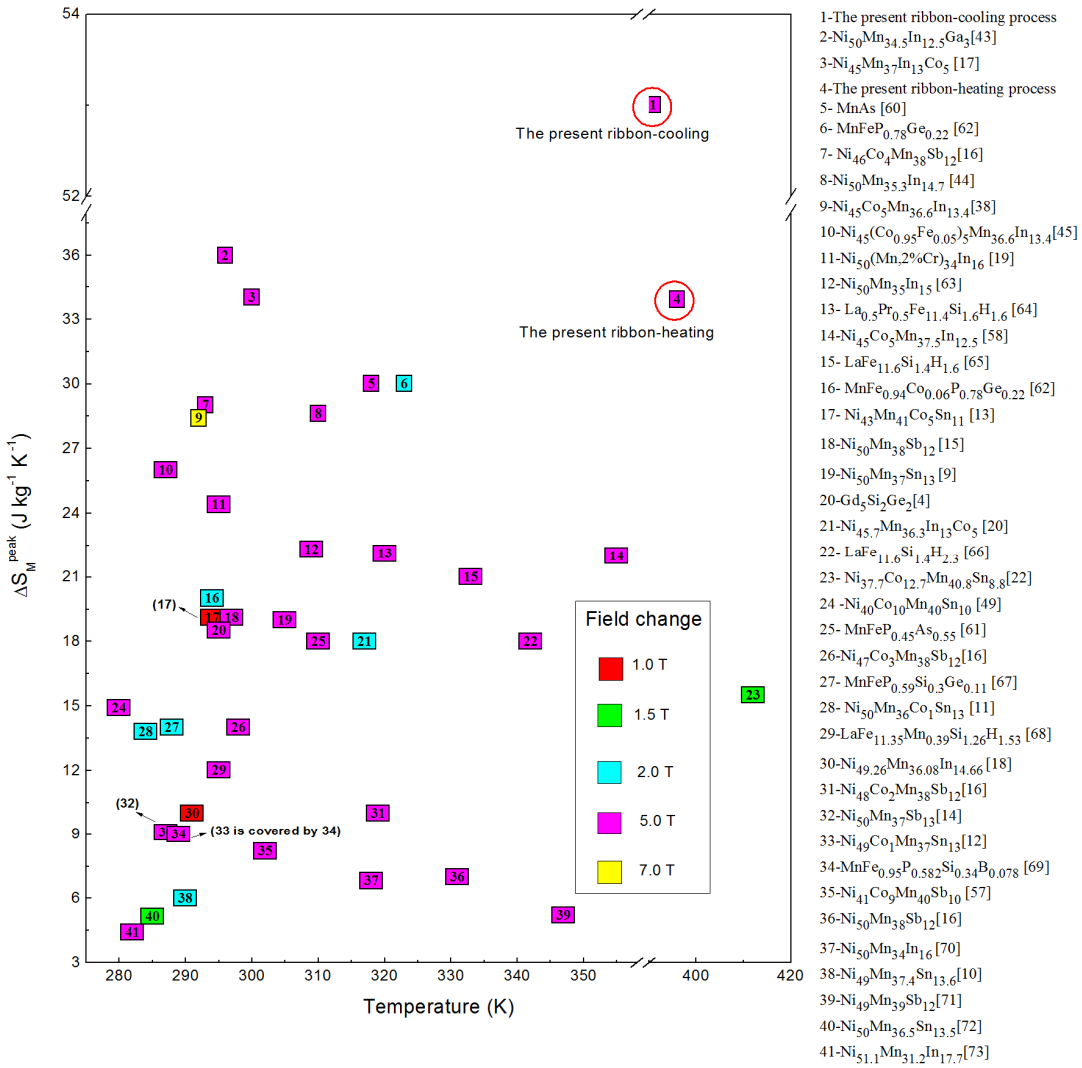

Fig. 9. $|\Delta S_M^{peak}|$ through the first-order structural transition around and above room temperature for Heusler alloys, $Gd_5Ge_2Si_2$, La(Fe, Si)$_{13}$-based alloys, and (Mn, Fe)$_2$P-type compounds [4, 9-20, 22, 38, 43-45, 49, 57, 58, 60-73]. The value of applied magnetic field change is distinguished by the filling color. For precise comparison, we select the data under a magnetic field of 5 T as far as possible. For sample 20, $|\Delta S_M^{peak}|$ is obtained upon cooling. Both samples 18 and 36 are $Ni_{50}Mn_{38}Sb_{12}$ but different results at different temperatures were reported by two laboratories. They are illustrated here together. Samples 33 and 34 are located at the same position in the figure. Note that the applied field for sample 33 is just 1 T, while 5 T for sample 34.

Highlights

1. The working temperature regime is far above room temperature.
2. Extremely large magnetic entropy changes are attained.
3. A negligible hysteresis loss is found upon forward martensitic transformation.